Simultaneous Tracking of Orbcomm LEO Satellites and Inertial Navigation System Aiding using Doppler Measurements

Joshua Morales[1], Joe Khalife[1], and Zaher M. Kassas[1,2]
[1]Department of Electrical Engineering and Computer Science, University of California, Irvine, USA
[2]Department of Mechanical and Aerospace Engineering, University of California, Irvine, USA
Emails: joshum9@uci.edu, khalifej@uci.edu, zkassas@ieee.org

***Abstract*—A framework for simultaneously tracking Orbcomm low Earth orbit (LEO) satellites and using Doppler measurements drawn from their signals to aid a vehicle's inertial navigation system (INS) is developed. The developed framework enables a navigating vehicle to exploit ambient Orbcomm LEO satellite signal Doppler measurements to aid its INS in a tightly-coupled fashion in the event global navigation satellite system (GNSS) signals become unusable. An overview of the extended Kalman filter-based simultaneous tracking and navigation (STAN) framework is provided. Experimental results are presented showing an unmanned aerial vehicle (UAV) aiding its INS with Doppler measurements drawn from two Orbcomm LEO satellites, reducing the final position error from 31.7 m to 8.9 m after 30 seconds of GNSS unavailability.**

I. Introduction

A global navigation satellite system (GNSS)-aided inertial navigation system (INS) makes use of the complementary properties of each individual system: the short-term accuracy and high data rates of an INS and the long-term stability of a GNSS solution to provide periodic corrections. However, in the inevitable event that GNSS signals become unavailable (e.g., in deep urban canyons, near dense foliage, and in the presence of unintentional interference or intentional jamming) or untrustworthy (e.g., during malicious spoofing attacks), the INS's errors will grow unboundedly.

Signals of opportunity (SOPs) have been considered as an alternative navigation source in the absence of GNSS signals [1], [2]. SOPs include AM/FM radio [3], cellular [4], [5], digital television [6], and low Earth orbit (LEO) satellites [7]–[9]. These signals have been demonstrated to yield a standalone meter-level-accurate navigation solution on ground vehicles [10]–[13] and a centimeter-level-accurate navigation solution on aerial vehicles [14], [15]. Moreover, these signals have been used as an aiding source for lidar [16], [17] and INS [18], [19].

LEO satellites are particularly attractive aiding sources for a vehicle's INS in GNSS-challenged environments for several reasons: (1) they are around twenty times closer to Earth compared to GNSS satellites which reside in medium Earth orbit (MEO), making their received signals between 300 to 2,400 times more powerful than GNSS signals [20]; (2) thousands of broadband internet satellites will be launched into LEO by OneWeb, SpaceX, Boeing, among others, bringing an abundance of signal sources [9]; and (3) each broadband provider will deploy satellites into unique orbital constellations transmitting at different frequency bands, making their signals diverse in frequency and direction [20].

To exploit LEO satellites for navigation, their positions and clock states, namely the clock bias and drift of the transmitter, must be known. The position of any satellite may be parameterized by its Keplerian elements: eccentricity, semi-major axis, inclination, longitude of the ascending node, argument of periapsis, and true anomaly. These elements are tracked, updated once daily, and made publicly available by the North American Aerospace Defense Command (NORAD) in the form of two-line element (TLE) files [21]. The information in these files are used to initialize a simplified general perturbation (SGP) model to propagate a satellite in its obit. However, the simplified models of perturbing forces, which include non-uniform Earth gravitational field, atmospheric drag, solar radiation pressure, third-body gravitational forces (e.g., gravity of the Moon and Sun), and general relativity [22], cause errors in a propagated satellite orbit as high as three kilometers. In contrast to GNSS, where corrections to the orbital elements and clock errors are periodically transmitted to the receiver in a navigation message, such orbital element and clock corrections may not be available for LEO satellites; in which case they must be estimated simultaneously with the navigating vehicle's states: orientation, position, velocity, inertial measurement unit (IMU) biases, and receiver's clock errors. The main contribution of this paper is to present a novel framework that estimates the LEO satellites' states simultaneously with the navigation vehicle's states and to demonstrate the framework's performance.

The exploitation of LEO satellites for navigation has been considered in other contexts. In [23], *simulated* LEO satellite Doppler measurements from *known* satellite positions were used to complement a cellular radio frequency pattern matching algorithm for localizing emergency 911 callers. In [24], *simulated* Doppler measurements from one LEO satellite with *known* position and velocity were used to localize a receiver. In [25], the position, velocity, and clock errors of a receiver were estimated using *simulated* LEO satellite time-difference of arrival (TDOA) and frequency-difference of arrival (FDOA) measurements using a reference receiver with a known posi-

tion. In contrast to these previous approaches which assumed perfectly known LEO satellite position states and used simulated measurements, the framework presented in this paper estimates the LEO satellites' position states along with the states of a navigating vehicle using *real* LEO satellite signals. A similar framework to estimate the position and clock states of *stationary* terrestrial transmitters while simultaneously aiding a vehicle's INS with pseudorange observables drawn from such transmitters was presented and studied in [18], [26]. This paper presents a more complex framework, which enables the tracking of *mobile* LEO transmitters' states. Specifically, a simultaneous tracking and navigation (STAN) framework is presented, which tracks the states of Orbcomm LEO satellites while simultaneously using Doppler measurements extracted from their signals to aid a vehicle's INS. A preliminary presentation of the framework was presented in [27], [28]; however, details of the framework were not provided. In this paper, details of the framework's components are discussed and its performance is demonstrated through an experiment on an unmanned aerial vehicle (UAV).

The remainder of this paper is organized as follows. Section II describes the LEO satellite signal-aided INS framework and discusses the LEO satellite dynamics model and the receiver measurement model. Section III provides an overview of the Orbcomm satellite system. Section IV presents experimental results demonstrating a UAV navigating with Orbcomm signals using the LEO satellite signal-aided INS framework. Concluding remarks are given in Section V.

II. STAN Navigation Framework

An extended Kalman filter (EKF) framework is employed to aid the INS with LEO satellite pseudorange rates and GNSS pseudoranges (when available) in a tightly-coupled fashion. The proposed STAN framework, illustrated in Fig. 1, works similarly to that of a traditional tightly-coupled GNSS-aided INS with two main differences: (i) the position and clock states of the LEO satellites are unknown to the vehicle-mounted receiver; hence, they are simultaneously estimated with the states of the navigating vehicle and (ii) Doppler measurements are used to aid the INS instead of GNSS pseudoranges. A similar framework was proposed in [18] to aid a vehicle's INS using stationary terrestrial emitters. The framework presented in this paper is more complex since it includes a LEO satellite dynamics model to propagate the positions of moving LEO satellites. The EKF state vector, state dynamics model, receiver's measurement model, and the EKF prediction and measurement update steps are discussed next.

A. EKF State Vector and Dynamics Model

1) EKF State Vector: The EKF state vector is given by

$$\boldsymbol{x} = \left[\, \boldsymbol{x}_{\mathrm{r}}^{\mathsf{T}},\, \boldsymbol{x}_{\mathrm{leo}_1}^{\mathsf{T}},\, \ldots,\, \boldsymbol{x}_{\mathrm{leo}_M}^{\mathsf{T}} \right]^{\mathsf{T}},$$

$$\boldsymbol{x}_{\mathrm{r}} = \left[{}_{G}^{B}\bar{\boldsymbol{q}}^{\mathsf{T}},\, \boldsymbol{r}_{\mathrm{r}}^{\mathsf{T}},\, \dot{\boldsymbol{r}}_{\mathrm{r}}^{\mathsf{T}},\, \boldsymbol{b}_{\mathrm{g}}^{\mathsf{T}},\, \boldsymbol{b}_{\mathrm{a}}^{\mathsf{T}},\, c\delta t_{\mathrm{r}},\, c\dot{\delta} t_{\mathrm{r}} \right]^{\mathsf{T}}$$

$$\boldsymbol{x}_{\mathrm{leo}_m} = \left[\boldsymbol{r}_{\mathrm{leo}_m}^{\mathsf{T}},\, \dot{\boldsymbol{r}}_{\mathrm{leo}_m}^{\mathsf{T}},\, c\delta t_{\mathrm{leo}_m},\, c\dot{\delta} t_{\mathrm{leo}_m} \right]^{\mathsf{T}},$$

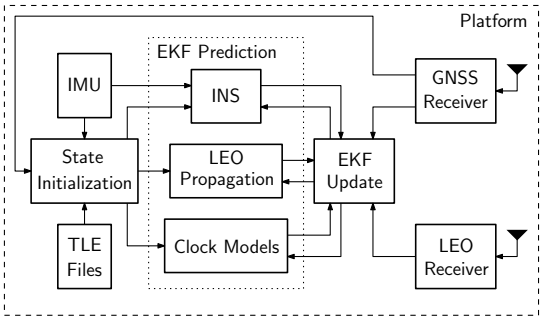

Fig. 1. Simultaneous LEO satellite tracking and navigation framework.

where $\boldsymbol{x}_{\mathrm{r}}$ is the state vector of the vehicle-mounted IMU and receiver which consists of ${}_{G}^{B}\bar{\boldsymbol{q}}$, which is a four-dimensional (4-D) unit quaternion representing the orientation of a body frame B fixed at the IMU with respect to a global frame G; $\boldsymbol{r}_{\mathrm{r}}$ and $\dot{\boldsymbol{r}}_{\mathrm{r}}$ are the three-dimensional (3-D) position and velocity of the IMU; $\boldsymbol{b}_{\mathrm{g}}$ and $\boldsymbol{b}_{\mathrm{a}}$ are 3-D biases of the IMU's gyroscopes and accelerometers, respectively; δt_{r} and $\dot{\delta} t_{\mathrm{r}}$ are the clock bias and drift of the receiver, respectively; and c is the speed of light. The vector $\boldsymbol{x}_{\mathrm{leo}_m}$ represents the states of the m^{th} LEO satellite, which consists of $\boldsymbol{r}_{\mathrm{leo}_m}$ and $\dot{\boldsymbol{r}}_{\mathrm{leo}_m}$, which are the 3-D satellite position and velocity, respectively; $\delta t_{\mathrm{leo}_m}$ and $\dot{\delta} t_{\mathrm{leo}_m}$ are the satellite's transceiver clock bias and drift, respectively; and $m = 1, \ldots, M$, with M being the total number of LEO satellites visible to the receiver.

2) Vehicle Dynamics Model: The vehicle's orientation, position, and velocity are modeled to evolve in time according to INS kinematic equations driven by a 3-D rotation rate vector ${}^{B}\boldsymbol{\omega}$ of the body frame and a 3-D acceleration vector ${}^{G}\boldsymbol{a}$ in the global frame. The gyroscopes' and accelerometers' biases are modeled to evolve according to the discrete-time (DT) dynamics, given by

$$\boldsymbol{b}_{\mathrm{g}}(k+1) = \boldsymbol{b}_{\mathrm{g}}(k) + \boldsymbol{w}_{\mathrm{bg}}(k) \tag{1}$$

$$\boldsymbol{b}_{\mathrm{a}}(k+1) = \boldsymbol{b}_{\mathrm{a}}(k) + \boldsymbol{w}_{\mathrm{ba}}(k), \quad k = 1, 2, \ldots \tag{2}$$

where $\boldsymbol{w}_{\mathrm{bg}}$ and $\boldsymbol{w}_{\mathrm{ba}}$ are process noise, which are modeled as DT white noise sequences with covariances $\mathbf{Q}_{\mathrm{bg}}$ and $\mathbf{Q}_{\mathrm{ba}}$, respectively. The vehicle-mounted receiver's clock error states are modeled to evolve in time according to

$$\boldsymbol{x}_{\mathrm{clk_r}}(k+1) = \mathbf{F}_{\mathrm{clk}}\, \boldsymbol{x}_{\mathrm{clk_r}}(k) + \boldsymbol{w}_{\mathrm{clk_r}}(k), \tag{3}$$

$$\boldsymbol{x}_{\mathrm{clk_r}} \triangleq \left[\, c\delta t_{\mathrm{r}},\, c\dot{\delta} t_{\mathrm{r}} \right]^{\mathsf{T}}, \quad \mathbf{F}_{\mathrm{clk}} = \begin{bmatrix} 1 & T \\ 0 & 1 \end{bmatrix},$$

where $\boldsymbol{w}_{\mathrm{clk_r}}$ is the process noise, which is modeled as a DT white noise sequence with covariance

$$\mathbf{Q}_{\mathrm{clk_r}} = \begin{bmatrix} S_{\tilde{w}_{\delta t_{\mathrm{r}}}} T + S_{\tilde{w}_{\dot{\delta} t_{\mathrm{r}}}} \frac{T^3}{3} & S_{\tilde{w}_{\dot{\delta} t_{\mathrm{r}}}} \frac{T^2}{2} \\ S_{\tilde{w}_{\dot{\delta} t_{\mathrm{r}}}} \frac{T^2}{2} & S_{\tilde{w}_{\dot{\delta} t_{\mathrm{r}}}} T \end{bmatrix}, \tag{4}$$

and T is the constant sampling interval [29]. The terms $S_{\tilde{w}_{\delta t_{\mathrm{r}}}}$ and $S_{\tilde{w}_{\dot{\delta} t_{\mathrm{r}}}}$ are the clock bias and drift process noise power spectra, respectively, which can be related to the power-law coefficients, $\{h_{\alpha,\mathrm{r}}\}_{\alpha=-2}^{2}$, which have been shown through laboratory experiments to characterize the power spectral

density of the fractional frequency deviation of an oscillator from nominal frequency according to $S_{\tilde{w}_{\delta t_\mathrm{r}}} \approx \frac{h_{0,\mathrm{r}}}{2}$ and $S_{\tilde{w}_{\dot{\delta} t_\mathrm{r}}} \approx 2\pi^2 h_{-2,\mathrm{r}}$ [30].

3) LEO Satellite Dynamics Model: The position and velocity dynamics of the m^{th} LEO satellite are modeled as the sum of the two-body motion model equation and other perturbing accelerations, given by

$$\ddot{\boldsymbol{r}}_{\mathrm{leo}_m}(t) = -\frac{\mu}{\|\boldsymbol{r}_{\mathrm{leo}_m}(t)\|_2^3}\boldsymbol{r}_{\mathrm{leo}_m}(t) + \tilde{\boldsymbol{a}}_{\mathrm{leo}_m}(t), \tag{5}$$

where $\ddot{\boldsymbol{r}}_{\mathrm{leo}_m} = \frac{d}{dt}\dot{\boldsymbol{r}}_{\mathrm{leo}_m}$, i.e., the acceleration of the m^{th} LEO satellite, μ is the standard gravitational parameter of Earth, and $\tilde{\boldsymbol{a}}_{\mathrm{leo}_m}$ captures the overall perturbation in acceleration, which includes perturbations caused by non-uniform Earth gravitational field, atmospheric drag, solar radiation pressure, third-body gravitational forces (e.g., gravity of the Moon and Sun), and general relativity [22]. The perturbation vector $\tilde{\boldsymbol{a}}_{\mathrm{leo}_m}$ is modeled as a white random process with power spectral density $\mathbf{Q}_{\tilde{a}_{\mathrm{leo}_m}}$. The m^{th} LEO satellite's clock states time evolution are modeled according to

$$\boldsymbol{x}_{\mathrm{clk}_{\mathrm{leo}_m}}(k+1) = \mathbf{F}_{\mathrm{clk}}\,\boldsymbol{x}_{\mathrm{clk}_{\mathrm{leo}_m}}(k) + \boldsymbol{w}_{\mathrm{clk}_{\mathrm{leo}_m}}(k), \tag{6}$$

where $\boldsymbol{w}_{\mathrm{clk}_{\mathrm{leo}_m}}$ is a DT white noise sequence with covariance of identical structure to $\mathbf{Q}_{\mathrm{clk}_\mathrm{r}}$ in (4), except that $S_{\tilde{w}_{\delta t_\mathrm{r}}}$ and $S_{\tilde{w}_{\dot{\delta} t_\mathrm{r}}}$ are replaced with the LEO satellite clock specific spectra $S_{\tilde{w}_{\delta t_{\mathrm{leo},m}}}$ and $S_{\tilde{w}_{\dot{\delta} t_{\mathrm{leo},m}}}$, respectively, where $S_{\tilde{w}_{\delta t_{\mathrm{leo},m}}} \approx \frac{h_{0,\mathrm{leo}_m}}{2}$ and $S_{\tilde{w}_{\dot{\delta} t_{\mathrm{leo},m}}} \approx 2\pi^2 h_{-2,\mathrm{leo}_m}$. The next section discusses how these models are used in the EKF prediction.

B. IMU Measurement Model and EKF Prediction

The vehicle-mounted IMU which contains a triad-gyroscope and a triad-accelerometer produces angular rate and specific force measurements, which are modeled as

$$\boldsymbol{\omega}_{\mathrm{imu}}(k) = {}^{B}\boldsymbol{\omega}(k) + \boldsymbol{b}_{\mathrm{g}}(k) + \boldsymbol{n}_{\mathrm{g}}(k) \tag{7}$$

$$\boldsymbol{a}_{\mathrm{imu}}(k) = \mathbf{R}\left[{}^{B}_{G}\bar{\boldsymbol{q}}(k)\right]\left({}^{G}\boldsymbol{a}(k) - {}^{G}\boldsymbol{g}(k)\right) + \boldsymbol{b}_{\mathrm{a}}(k) + \boldsymbol{n}_{\mathrm{a}}(k), \tag{8}$$

where ${}^{G}\boldsymbol{g}$ is the acceleration due to gravity in the global frame and $\boldsymbol{n}_{\mathrm{g}}$ and $\boldsymbol{n}_{\mathrm{a}}$ are measurement noise vectors, which are modeled as white noise sequences with covariances $\sigma_{\mathrm{g}}^2\mathbf{I}_{3\times3}$ and $\sigma_{\mathrm{g}}^2\mathbf{I}_{3\times3}$, respectively.

The EKF prediction step produces $\hat{\boldsymbol{x}}(k|j) \triangleq \mathbb{E}[\boldsymbol{x}(k)|\boldsymbol{Z}^j]$ of $\boldsymbol{x}(k)$, and an associated estimation error covariance $\mathbf{P}_{\boldsymbol{x}}(k|j)$, where $\mathbb{E}[\cdot|\cdot]$ is the conditional expectation operator, $\boldsymbol{Z}^j \triangleq \{\boldsymbol{z}(i)\}_{i=1}^{j}$ are the set of measurements available up to and including time index j, and $k > j$. The measurements available $\boldsymbol{z}$ will be discussed in the next subsection.

The IMU measurements (7) and (8) are processed through strapdown INS equations using an Earth-centered Earth-fixed (ECEF) frame as frame G to produce ${}^{B}_{G}\hat{\bar{\boldsymbol{q}}}(k|j)$, $\hat{\boldsymbol{r}}_{\mathrm{r}}(k|j)$, and $\hat{\dot{\boldsymbol{r}}}_{\mathrm{r}}(k|j)$ [31]. The gyroscopes' and accelerometers' biases predictions $\hat{\boldsymbol{b}}_{\mathrm{g}}(k|j)$ and $\hat{\boldsymbol{b}}_{\mathrm{a}}(k|j)$ follow from (1) and (2), respectively. The prediction of the clock states of both the receiver and the LEO satellite transceivers follow from (3) and (6), respectively. The prediction of the LEO satellites' position and velocity is performed by linearizing and discretizing (5). Next, the measurement model and the EKF measurement update is described.

C. Receiver Measurement Model and EKF Update

The GNSS receiver makes pseudorange measurements at DT instants on all available GNSS satellites, which after compensating for ionospheric and tropospheric delays is given by

$$\begin{aligned} z_{\mathrm{gnss}_l}(j) = {} & \|\boldsymbol{r}_{\mathrm{r}}(j) - \boldsymbol{r}_{\mathrm{gnss}_l}(j)\|_2 \\ & + c\cdot\left[\delta t_{\mathrm{r}}(j) - \delta t_{\mathrm{gnss}_l}(j)\right] + v_{\mathrm{gnss}_l}(j),\ j = 1, 2, \ldots \end{aligned} \tag{9}$$

where $z_{\mathrm{gnss}_l} \triangleq z'_{\mathrm{gnss}_l} - c\delta t_{\mathrm{iono}} - c\delta t_{\mathrm{tropo}}$; δt_{iono} and $\delta t_{\mathrm{tropo}}$ are the ionospheric and tropospheric delays, respectively; z'_{gnss_l} is the uncompensated pseudorange; v_{gnss_l} is the measurement noise, which is modeled as a DT zero-mean white Gaussian sequence with variance $\sigma^2_{\mathrm{gnss}_l}$; and $l = 1, \ldots, L$, with L being the total number of GNSS satellites.

The LEO receiver makes Doppler frequency measurements f_D on the available LEO satellite signals, from which a pseudorange rate measurement $\dot{\rho}_{\mathrm{leo}}$ can be obtained from $\dot{\rho}_{\mathrm{leo}} = -\frac{c}{f_c}f_D$, where f_c is the carrier frequency. The pseudorange rate measurement $\dot{\rho}_{\mathrm{leo}_m}$ from the m^{th} LEO satellite is modeled according to

$$\begin{aligned} \dot{\rho}_{\mathrm{leo}_m}(j) = {} & \left[\dot{\boldsymbol{r}}_{\mathrm{leo}_m}(j) - \dot{\boldsymbol{r}}_r(j)\right]^{\mathsf{T}} \frac{\left[\boldsymbol{r}_r(j) - \boldsymbol{r}_{\mathrm{leo}_m}(j)\right]}{\|\boldsymbol{r}_r(j) - \boldsymbol{r}_{\mathrm{leo}_m}(j)\|_2} \\ & + c\cdot\left[\dot{\delta}t_r(j) - \dot{\delta}t_{\mathrm{leo}_m}(j)\right] + c\dot{\delta}t_{\mathrm{iono}_m}(j) \\ & + c\dot{\delta}t_{\mathrm{tropo}_m}(j) + v_{\mathrm{leo}_m}(j), \end{aligned}$$

where $\dot{\delta}t_{\mathrm{iono}_m}$ and $\dot{\delta}t_{\mathrm{tropo}_m}$ are the drifts of the ionospheric and tropospheric delays, respectively, for the m^{th} LEO satellite; and v_{leo_m} is the measurement noise, which is modeled as a white Gaussian random sequence with variance $\sigma^2_{\mathrm{leo}_m}$. Note that the variation in the ionospheric and tropospheric delays during LEO satellite visibility is negligible compared to the errors in the satellite's estimated velocities [32]; hence, $\dot{\delta}t_{\mathrm{iono}_m}$ and $\dot{\delta}t_{\mathrm{tropo}_m}$ are ignored in the measurement, yielding the measurement model given by

$$\begin{aligned} \dot{\rho}_{\mathrm{leo}_m}(j) \approx {} & \left[\dot{\boldsymbol{r}}_{\mathrm{leo}_m}(j) - \dot{\boldsymbol{r}}_r(j)\right]^{\mathsf{T}} \frac{\left[\boldsymbol{r}_r(j) - \boldsymbol{r}_{\mathrm{leo}_m}(j)\right]}{\|\boldsymbol{r}_r(j) - \boldsymbol{r}_{\mathrm{leo}_m}(j)\|_2} \\ & + c\cdot\left[\dot{\delta}t_r(j) - \dot{\delta}t_{\mathrm{leo}_m}(j)\right] + v_{\mathrm{leo}_m}(j). \end{aligned} \tag{10}$$

The STAN framework operates in a tracking mode when GNSS measurements are available and a STAN mode when GNSS signals are unavailable. In the tracking mode, the measurement vector $\boldsymbol{z}$ processed by the EKF update is defined by stacking all available GNSS pseudoranges and LEO satellite Doppler measurements and is given by

$$\boldsymbol{z} \triangleq \left[\boldsymbol{z}_{\mathrm{gnss}}^{\mathsf{T}},\, \dot{\boldsymbol{\rho}}_{\mathrm{leo}}^{\mathsf{T}}\right]^{\mathsf{T}}, \tag{11}$$

$$\boldsymbol{z}_{\mathrm{gnss}} \triangleq \left[z_{\mathrm{gnss}_1}, \ldots, z_{\mathrm{gnss}_L}\right]^{\mathsf{T}}, \quad \dot{\boldsymbol{\rho}}_{\mathrm{leo}} \triangleq \left[\dot{\rho}_{\mathrm{leo}_1}, \ldots, \dot{\rho}_{\mathrm{leo}_M}\right]^{\mathsf{T}}.$$

The EKF measurement update step produces $\hat{\boldsymbol{x}}(j|j)$ and an associated posterior estimation error covariance $\mathbf{P}_{\boldsymbol{x}}(j|j)$. The corresponding measurement Jacobian of $\boldsymbol{z}$ is given by

$$\mathbf{H} = \left[\mathbf{H}_{\boldsymbol{z}_{\text{gnss}}}^{\mathsf{T}},\, \mathbf{H}_{\dot{\boldsymbol{\rho}}_{\text{leo}}}^{\mathsf{T}}\right]^{\mathsf{T}}, \tag{12}$$

where $\mathbf{H}_{\boldsymbol{z}_{\text{gnss}}}$ is the measurement Jacobian of $\boldsymbol{z}_{\text{gnss}}$, which is given by

$$\mathbf{H}_{\boldsymbol{z}_{\text{gnss}}} = \begin{bmatrix} \mathbf{0}_{1\times 3} & \boldsymbol{h}_{\text{gnss}_1}^{\mathsf{T}} & \mathbf{0}_{1\times 9} & \boldsymbol{h}_{\text{clk}}^{\mathsf{T}} & \mathbf{0}_{1\times 8M} \\ \vdots & \vdots & \vdots & \vdots & \vdots \\ \mathbf{0}_{1\times 3} & \boldsymbol{h}_{\text{gnss}_L}^{\mathsf{T}} & \mathbf{0}_{1\times 9} & \boldsymbol{h}_{\text{clk}}^{\mathsf{T}} & \mathbf{0}_{1\times 8M} \end{bmatrix},$$

where

$$\boldsymbol{h}_{\text{gnss}_l} = \frac{\hat{\boldsymbol{r}}_r - \boldsymbol{r}_{\text{gnss}_l}}{\|\hat{\boldsymbol{r}}_r - \boldsymbol{r}_{\text{gnss}_l}\|}, \quad \boldsymbol{h}_{\text{clk}} = \begin{bmatrix} 1 \\ 0 \end{bmatrix}.$$

The measurement Jacobian of $\dot{\boldsymbol{\rho}}_{\text{leo}}$ is given by

$$\mathbf{H}_{\dot{\boldsymbol{\rho}}_{\text{leo}}} = \begin{bmatrix} \mathbf{H}_{\dot{\boldsymbol{\rho}}_{\text{leo}},r} & \mathbf{H}_{\dot{\boldsymbol{\rho}},\text{leo}} \end{bmatrix},$$

$$\mathbf{H}_{\dot{\boldsymbol{\rho}}_{\text{leo}},r} = \begin{bmatrix} \mathbf{0}_{1\times 3} & -(\boldsymbol{h}_{v_{\text{leo}_1}}^{\mathsf{T}} - \boldsymbol{h}_{r_{\text{leo}_1}}^{\mathsf{T}} \boldsymbol{h}_{v_{\text{leo}_1}} \boldsymbol{h}_{r_{\text{leo}_1}}^{\mathsf{T}}) & -\boldsymbol{h}_{r_{\text{leo}_1}}^{\mathsf{T}} & \boldsymbol{b}^{\mathsf{T}} \\ \vdots & \vdots & \vdots & \vdots \\ \mathbf{0}_{1\times 3} & -(\boldsymbol{h}_{v_{\text{leo}_M}}^{\mathsf{T}} - \boldsymbol{h}_{r_{\text{leo}_1}}^{\mathsf{T}} \boldsymbol{h}_{v_{\text{leo}_M}} \boldsymbol{h}_{r_{\text{leo}_M}}^{\mathsf{T}}) & -\boldsymbol{h}_{r_{\text{leo}_M}}^{\mathsf{T}} & \boldsymbol{b}^{\mathsf{T}} \end{bmatrix},$$

$$\boldsymbol{h}_{r_{\text{leo}_m}} = \frac{\hat{\boldsymbol{r}}_r - \hat{\boldsymbol{r}}_{\text{leo}_m}}{\|\hat{\boldsymbol{r}}_r - \hat{\boldsymbol{r}}_{\text{leo}_m}\|}, \quad \boldsymbol{h}_{v_{\text{leo}_m}} = \frac{\hat{\dot{\boldsymbol{r}}}_r - \hat{\dot{\boldsymbol{r}}}_{\text{leo}_m}}{\|\hat{\boldsymbol{r}}_r - \hat{\boldsymbol{r}}_{\text{leo}_m}\|},$$

$$\boldsymbol{b} = [\,\mathbf{0}_{1\times 7}, 1\,]^{\mathsf{T}}, \quad \mathbf{H}_{\dot{\boldsymbol{\rho}},\text{leo}} = \text{diag}\,[\mathbf{H}_{\dot{\boldsymbol{\rho}},\text{leo}_1}, \ldots, \mathbf{H}_{\dot{\boldsymbol{\rho}},\text{leo}_M}],$$

$$\mathbf{H}_{\dot{\boldsymbol{\rho}},\text{leo}_m} = \begin{bmatrix} (\boldsymbol{h}_{v_{\text{leo}_m}}^{\mathsf{T}} - \boldsymbol{h}_{r_{\text{leo}_m}}^{\mathsf{T}} \boldsymbol{h}_{v_{\text{leo}_m}} \boldsymbol{h}_{r_{\text{leo}_m}}^{\mathsf{T}}) & \boldsymbol{h}_{r_{\text{leo}_m}}^{\mathsf{T}} & 0 & -1 \end{bmatrix}.$$

When GNSS measurements become unavailable, the framework switches to the STAN mode, at which point the measurement vector (11) and the measurement Jacobian (12) are replaced with $\boldsymbol{z}' = \dot{\boldsymbol{\rho}}_{\text{leo}}$ and $\mathbf{H}' = \mathbf{H}_{\dot{\boldsymbol{\rho}}_{\text{leo}}}$, respectively. The next section discusses the Orbcomm LEO satellite constellation from which the Doppler measurements were drawn to aid the INS in the UAV experiment presented in Section IV.

III. Orbcomm System

This section gives an overview of the Orbcomm satellite constellation and discusses the signals that were exploited to the INS.

A. Orbcomm System Overview

The Orbcomm system is a wide area two-way communication system that uses a constellation of LEO satellites to provide worldwide geographic coverage for sending and receiving alphanumeric packets [33]. The Orbcomm system consists of three main components: (i) subscriber communicators (users), (ii) ground segment (gateways), and (iii) space segment (constellation of satellites), which are briefly discussed next.

(i) Subscriber Communicators (SCs): There are several types of SCs. Orbcomm's SC for fixed data applications uses low-cost, very high frequency (VHF) electronics. The SC for mobile two-way messaging is a hand-held, stand-alone unit.

(ii) Ground Segment: The ground segment consists of gateway control centers (GCCs), gateway Earth stations (GESs), and the network control center (NCC). The GCC provides switching capabilities to link mobile SCs with terrestrial based customer systems via standard communications modes. GESs link the ground segment with the space segment. GESs mainly track and monitor satellites based on orbital information from the GCC and transmit to and receive from satellites, the GCC, or the NCC. The NCC is responsible for managing the Orbcomm network elements and the gateways through telemetry monitoring, system commanding, and mission system analysis.

(iii) Space Segment: Orbcomm satellites are used to complete the link between the SCs and the switching capability at the NCC or GCC.

B. Orbcomm LEO Satellite Constellation

The Orbcomm constellation, at maximum capacity, has up to 47 satellites in 7 orbital planes A–G, illustrated in Fig. 2. Planes A, B, and C are inclined at 45° to the equator and each contains 8 satellites in a circular orbit at an altitude of approximately 815 km. Plane D, also inclined at 45°, contains 7 satellites in a circular orbit at an altitude of 815 km. Plane E is inclined at 0° and contains 7 satellites in a circular orbit at an altitude of 975 km. Plane F is inclined at 70° and contains 2 satellites in a near-polar circular orbit at an altitude of 740 km. Plane G is inclined at 108° and contains 2 satellites in a near-polar elliptical orbit at an altitude varying between 785 km and 875 km.

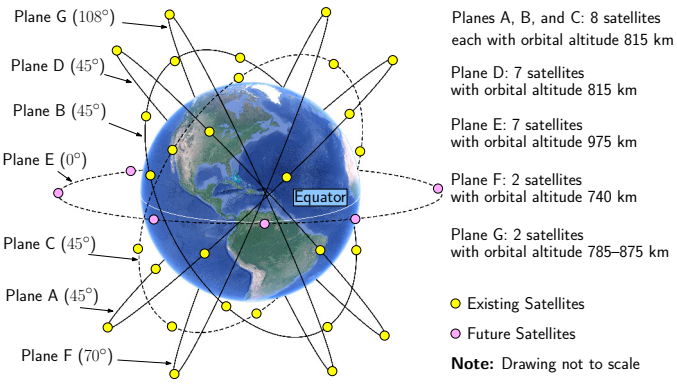

Fig. 2. Orbcomm LEO satellite constellation. Map data: Google Earth.

C. Orbcomm Downlink Signals

The LEO receiver draws pseudorange rate observables from Orbcomm LEO signals on the downlink channel. Satellite radio frequency (RF) downlinks to SCs and GESs are within the 137–138 MHz VHF band. Downlink channels include 12 channels for transmitting to SCs and one gateway channel, which is reserved for transmitting to the GESs. Each satellite

transmits to SCs on one of the 12 subscriber downlink channels through a frequency-sharing scheme that provides four-fold channel reuse. The Orbcomm satellites have a subscriber transmitter that provides a continuous 4800 bits-per-second (bps) stream of packet data using symmetric differential-quadrature phase shift keying (SD-QPSK). Each satellite also has multiple subscriber receivers that receive short bursts from the SCs at 2400 bps.

Note that Orbcomm satellites are also equipped with a specially constructed 1-Watt ultra high frequency (UHF) transmitter that is designed to emit a highly stable signal at 400.1 MHz. The transmitter is coupled to a UHF antenna designed to have a peak gain of approximately 2 dB. The UHF signal is used by the Orbcomm system for SC positioning. However, experimental data shows that the UHF beacon is absent. Moreover, even if the UHF beacon was present, one would need to be a paying subscriber to benefit from positioning services. Consequently, only downlink channel VHF signals are exploited to aid the INS.

IV. Experimental Results

This section presents experimental results of a UAV navigating with the proposed STAN framework. First, the experimental setup is described, then experimental results are provided.

A. Experimental Setup

An experimental test was conducted in Riverside, California to evaluate the performance of the proposed LEO signal-aided INS STAN framework. To this end, a DJI Matrice 600 UAV was equipped with following hardware and software setup:

- A low-cost VHF dipole antenna.
- An RTL-SDR dongle to sample Orbcomm signals.
- A laptop computer to store the sampled Orbcomm signals. These samples were then processed by the Multi-channel Adaptive TRansceiver Information eXtractor (MATRIX) software-defined quadrature phase-shift keying (QPSK) receiver developed by the Autonomous Systems Perception, Intelligence, and Navigation (ASPIN) Laboratory to perform carrier synchronization and extract pseudorange rate observables [34].
- A Septentrio AsteRx-i V integrated GNSS-IMU, which is equipped with a dual-antenna, multi-frequency GNSS receiver and a Vectornav VN-100 micro-electromechanical system (MEMS) IMU. Septentrio's post-processing software development kit (PP-SDK) was used to process Global Position System (GPS) carrier phase observables collected by the AsteRx-i V and by a nearby differential GPS base station to obtain a carrier phase-based navigation solution. This integrated GNSS-IMU real-time kinematic (RTK) system [35] was used to produce the ground truth results with which the proposed navigation framework was compared.

The experimental setup is shown in Fig. 3.

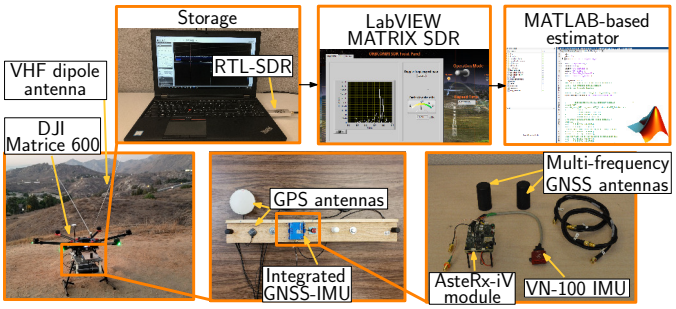

Fig. 3. Experimental setup.

B. Results

The UAV flew a commanded trajectory over a 120-second period during which 2 Orbcomm LEO satellites were available. Two estimators were implemented to estimate the flown trajectories: (i) the LEO signal-aided INS STAN framework described in Section II and (ii) a traditional GPS-aided INS for comparative analysis.

The receiver clock was modeled to be equipped with a typical temperature-compensated crystal oscillator (TCXO), with $\{h_{0,r}, h_{-2,r}\} = \{9.4 \times 10^{-20}, 3.8 \times 10^{-21}\}$. The values $\{h_{0,\text{leo}_m}, h_{-2,\text{leo}_m}\}_{m=1}^{2}$ corresponding to the LEO satellites' clocks were solved for online while GPS signals were still available. The measurement noise variances of the LEO satellite signal Doppler measurements $\left\{\sigma^2_{\text{leo}_m}\right\}_{m=1}^{2}$ were determined empirically offline while GPS measurements were still available. The initial estimates of the position and velocity for each Orbcomm LEO satellite were found using an SGP model and TLE files downloaded on June 15, 2018. The corresponding initial estimation error 1-standard deviations for each satellite were set to $(3 \times 10^3) \cdot \mathbf{I}_{3\times 3}$ m and $100 \cdot \mathbf{I}_{3\times 3}$ m/s for the position and velocity, respectively, where $\mathbf{I}_{3\times 3}$ is a 3×3 identity matrix. The UAV's position and velocity and their corresponding uncertainties were initialized using the Septentrio AsteRx-i V integrated GNSS-IMU solution and associated estimation error covariance, respectively.

Each estimator had access to GPS for only the first 90 seconds of the run as illustrated in Fig. 4 (d). Fig. 4 (a) shows the trajectory of the 2 Orbcomm LEO satellites traversed over the course of the experiment. The 3-D position root mean-squared error (RMSE) of the traditional GPS-aided INS's navigation solution after GPS became unavailable was 14.4 meters with a final error of 31.7 meters. The 3-D position RMSE of the UAV's trajectory for the LEO signal-aided INS was 6.8 meters with a final error of 8.8 meters. The estimated satellite trajectory and the along-track, radial, cross-track 95^{th}-percentile final uncertainty ellipsoid of one of the satellite's position states are illustrated in Fig. 4 (b).

V. Conclusions

This work presented a STAN framework which simultaneously tracks LEO satellites and uses Doppler measurements drawn from their signals for aiding a vehicle's INS in the absence of GNSS signals. An overview of the EKF-based

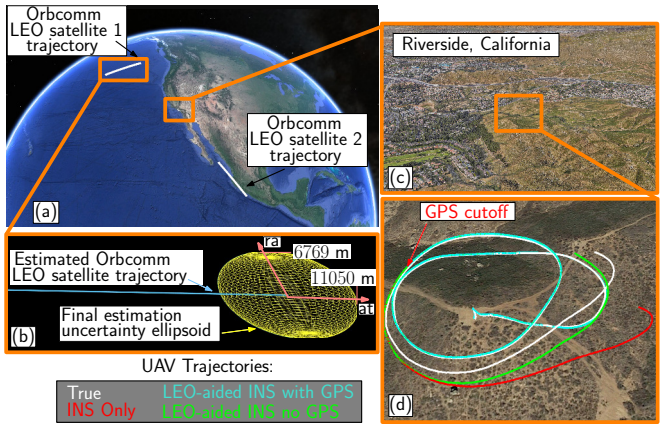

Fig. 4. Experimental results showing (a) the trajectory of the 2 Orbcomm LEO satellites; (b) estimated trajectory of one of the satellites and the final along-track (at), radial (ra), and cross-track (ct) position uncertainty; and (c)–(d) true and estimated trajectories of the UAV.

STAN framework and the LEO Orbcomm satellite system was provided. Moreover, experimental results were presented demonstrating a UAV navigating using 2 Orbcomm satellite signals in the absence of GNSS. It was demonstrated that the developed framework reduced the UAV's final position error by 72.2% compared to an unaided INS after 30 seconds of GNSS unavailability.

Acknowledgment

This work was supported in part by the Office of Naval Research (ONR) under Grant N00014-16-1-2305 and in part by the National Science Foundation (NSF) under Grant 1751205.

References

[1] L. Merry, R. Faragher, and S. Schedin, "Comparison of opportunistic signals for localisation," in *Proceedings of IFAC Symposium on Intelligent Autonomous Vehicles*, September 2010, pp. 109–114.

[2] Z. Kassas, "Collaborative opportunistic navigation," *IEEE Aerospace and Electronic Systems Magazine*, vol. 28, no. 6, pp. 38–41, 2013.

[3] J. McElroy, "Navigation using signals of opportunity in the AM transmission band," Master's thesis, Air Force Institute of Technology, Wright-Patterson Air Force Base, Ohio, USA, 2006.

[4] Z. Kassas, J. Khalife, K. Shamaei, and J. Morales, "I hear, therefore I know where I am: Compensating for GNSS limitations with cellular signals," *IEEE Signal Processing Magazine*, pp. 111–124, September 2017.

[5] K. Shamaei, J. Khalife, and Z. Kassas, "Exploiting LTE signals for navigation: Theory to implementation," *IEEE Transactions on Wireless Communications*, vol. 17, no. 4, pp. 2173–2189, April 2018.

[6] P. Thevenon, S. Damien, O. Julien, C. Macabiau, M. Bousquet, L. Ries, and S. Corazza, "Positioning using mobile TV based on the DVB-SH standard," *NAVIGATION, Journal of the Institute of Navigation*, vol. 58, no. 2, pp. 71–90, 2011.

[7] M. Rabinowitz, B. Parkinson, C. Cohen, M. O'Connor, and D. Lawrence, "A system using LEO telecommunication satellites for rapid acquisition of integer cycle ambiguities," in *Proceedings of IEEE/ION Position Location and Navigation Symposium*, April 1998, pp. 137–145.

[8] M. Joerger, L. Gratton, B. Pervan, and C. Cohen, "Analysis of Iridium-augmented GPS for floating carrier phase positioning," *NAVIGATION, Journal of the Institute of Navigation*, vol. 57, no. 2, pp. 137–160, 2010.

[9] T. Reid, A. Neish, T. Walter, and P. Enge, "Broadband LEO constellations for navigation," *NAVIGATION, Journal of the Institute of Navigation*, vol. 65, no. 2, pp. 205–220, 2018.

[10] C. Yang, T. Nguyen, and E. Blasch, "Mobile positioning via fusion of mixed signals of opportunity," *IEEE Aerospace and Electronic Systems Magazine*, vol. 29, no. 4, pp. 34–46, April 2014.

[11] J. Khalife and Z. Kassas, "Navigation with cellular CDMA signals – part II: Performance analysis and experimental results," *IEEE Transactions on Signal Processing*, vol. 66, no. 8, pp. 2204–2218, April 2018.

[12] M. Driusso, C. Marshall, M. Sabathy, F. Knutti, H. Mathis, and F. Babich, "Vehicular position tracking using LTE signals," *IEEE Transactions on Vehicular Technology*, vol. 66, no. 4, pp. 3376–3391, April 2017.

[13] K. Shamaei and Z. Kassas, "LTE receiver design and multipath analysis for navigation in urban environments," *NAVIGATION, Journal of the Institute of Navigation*, vol. 65, no. 4, pp. 655–675, December 2018.

[14] J. Khalife and Z. Kassas, "Precise UAV navigation with cellular carrier phase measurements," in *Proceedings of IEEE/ION Position, Location, and Navigation Symposium*, April 2018, pp. 978–989.

[15] J. Khalife, K. Shamaei, S. Bhattacharya, and Z. Kassas, "Centimeter-accurate UAV navigation with cellular signals," in *Proceedings of ION GNSS Conference*, September 2018, pp. 2321–2331.

[16] J. Khalife, S. Ragothaman, and Z. Kassas, "Pose estimation with lidar odometry and cellular pseudoranges," in *Proceedings of IEEE Intelligent Vehicles Symposium*, June 2017, pp. 1722–1727.

[17] M. Maaref, J. Khalife, and Z. Kassas, "Lane-level localization and mapping in GNSS-challenged environments by fusing lidar data and cellular pseudoranges," *IEEE Transactions on Intelligent Vehicles*, vol. 4, no. 1, pp. 73–89, March 2019.

[18] J. Morales, P. Roysdon, and Z. Kassas, "Signals of opportunity aided inertial navigation," in *Proceedings of ION GNSS Conference*, September 2016, pp. 1492–1501.

[19] Z. Kassas, J. Morales, K. Shamaei, and J. Khalife, "LTE steers UAV," *GPS World Magazine*, vol. 28, no. 4, pp. 18–25, April 2017.

[20] D. Lawrence, H. Cobb, G. Gutt, M. OConnor, T. Reid, T. Walter, and D. Whelan, "Navigation from LEO: Current capability and future promise," *GPS World Magazine*, vol. 28, no. 7, pp. 42–48, July 2017.

[21] North American Aerospace Defense Command (NORAD), "Two-line element sets," http://celestrak.com/NORAD/elements/.

[22] J. Vetter, "Fifty years of orbit determination: Development of modern astrodynamics methods," *Johns Hopkins APL Technical Digest*, vol. 27, no. 3, pp. 239–252, November 2007.

[23] D. Qiu, D. Lorenzo, and T. Bhattacharya, "Indoor geo-location with cellular rf pattern matching and LEO communication satellite signals," in *Proceedings of ION International Technical Meeting Conference*, January 2013, pp. 726–733.

[24] X. Chen, M. Wang, and L. Zhang, "Analysis on the performance bound of Doppler positioning using one LEO satellite," in *Proceedings of IEEE Vehicular Technology Conference*, May 2016, pp. 1–5.

[25] J. Zhao, L. Li, and Y. Gong, "Joint navigation and synchronization in LEO dual-satellite geolocation systems," in *Proceedings of IEEE Vehicular Technology Conference*, June 2017, pp. 1–5.

[26] J. Morales and Z. Kassas, "A low communication rate distributed inertial navigation architecture with cellular signal aiding," in *Proceedings of IEEE Vehicular Technology Conference*, 2018, pp. 1–6.

[27] J. Morales, J. Khalife, A. Abdallah, C. Ardito, and Z. Kassas, "Inertial navigation system aiding with Orbcomm LEO satellite Doppler measurements," in *Proceedings of ION GNSS Conference*, September 2018, pp. 2718–2725.

[28] C. Ardito, J. Morales, J. Khalife, A. Abdallah, and Z. Kassas, "Performance evaluation of navigation using LEO satellite signals with periodically transmitted satellite positions," in *Proceedings of ION International Technical Meeting Conference*, 2019, accepted.

[29] Z. Kassas and T. Humphreys, "Observability analysis of collaborative opportunistic navigation with pseudorange measurements," *IEEE Transactions on Intelligent Transportation Systems*, vol. 15, no. 1, pp. 260–273, February 2014.

[30] A. Thompson, J. Moran, and G. Swenson, *Interferometry and Synthesis in Radio Astronomy*, 2nd ed. John Wiley & Sons, 2001.

[31] P. Groves, *Principles of GNSS, Inertial, and Multisensor Integrated Navigation Systems*, 2nd ed. Artech House, 2013.

[32] P. Misra and P. Enge, *Global Positioning System: Signals, Measurements, and Performance*, 2nd ed. Ganga-Jamuna Press, 2010.

[33] Orbcomm, https://www.orbcomm.com/en/networks/satellite, accessed September 30, 2018.

[34] J. Khalife and Z. Kassas, "Receiver design for Doppler positioning with LEO satellites," in *Proceedings of IEEE International Conference on Acoustics, Speech and Signal Processing*, 2019, accepted.

[35] (2018) Septentrio AsteRx-i V. [Online]. Available: https://www.septentrio.com/products